
Natural Convection Heat Transfer in Roofs with Above-Sheathing Ventilation

William Miller, PhD
Member ASHRAE

Majid Keyhani, PhD

Timothy Stovall

Adam Youngquist

ABSTRACT

An algorithm was developed for predicting the rates of airflow and heat flow in an inclined air space heated from above or from below. The algorithm yields the mass flow rate and the temperature rise of the thermally induced flow rate. The flow and convective heat transfer are very similar to those occurring in inclined cooling ducts formed by offset roof-mounted photovoltaic installations. The algorithm is useful for predicting the free laminar convection heat transfer prevalent in roofs elevated from the roof deck. The routine was implemented in an attic simulation code and validated against thermal field data for stone-coated metal roofs equipped with above-sheathing ventilation.

INTRODUCTION

The old adage “keeping a roof over one’s head” aptly describes the basic human need for shelter. A roof provides protection from the sun, wind, and rain. It is designed to prevent or limit the flow of mass and energy, depending on the environmental differences between the conditioned space and the outdoor ambient. Craftsmen at some point during the evolution of building discovered the water-shedding qualities of different materials, including overlapped slate and stone slabs. Where natural slabs were scarce, clay was used, and the first single-lap roof tiles were molded by hand and shaped over the thighs of female artisans. Even today, some Spanish tile have this characteristic shape, wide at one end and narrow at the other (Baker 1980). The Chinese made clay tile roofs about 5000 years ago, as did people of the Middle East a short time later. Terra-cotta tile have also been found in Greek ruins dating more than a thousand years B.C. As craftsmen progressed in knowledge, guided by practical rules of experience, material and design improvements were made in roof systems. Interestingly, the original molding of tile led to a serendipitous design that enhanced both the energy efficiency and the durability of roofs. The air space formed by the single-lap tile combined with the introduction of plywood decking

(Rose 1995) provided a path for natural ventilation above the sheathing.

Placing tile and stone-coated metal roofs on batten and counter-batten supports provides excellent thermal performance, although it is not the current practice used in Florida or in California because of concerns about wind uplift during storms. Counter-batten construction provides an air space between the exterior face of the roof sheathing and the underside of the roof cover so that a clear, albeit complex, air pathway exists beneath the roof cover from the soffit to the ridge of the roof. Solar irradiance absorbed at the roof’s surface is conducted through the roof and convected as heat to the air. The warmer – and therefore, more buoyant – air moves up the inclined air passage. Miller, Wilson, and Karagiozis (2006) observed that the ventilation scheme helped remove unwanted heat and moisture from the roof deck, thereby improving the roof’s thermal performance as well as its durability. The thermally induced airflow occurring in this air space is termed above-sheathing ventilation (ASV).

ABOVE SHEATHING VENTILATION—FIELD DATA

Beal and Chandra (1995) did some of the first definitive studies of concrete tile roofs exhibiting ASV. Two identical

William Miller is a mechanical engineer for the Engineering Science and Technology Division of the Oak Ridge National Laboratory, Oak Ridge, TN. **Majid Keyhani** is a professor and **Adam Youngquist** is a graduating student in the department of Mechanical Engineering at University of Tennessee, Knoxville, TN. **Timothy Stovall** is a graduate student in the department of Mechanical Engineering, University of Colorado, Boulder, CO.

medium-profile concrete tile roofs were installed and compared with an adjacent asphalt shingle roof. One tile roof was direct-nailed. Its ridge was sealed with concrete mud and the soffit plugged with bird stops. The other concrete tile roof was offset mounted about 1½ in. above the deck using a batten and counter-batten system. The ridge and soffit were open to maximize ventilation under the tile. Beal and Chandra (1995) measured a 48% reduction in the daytime heat flux penetrating the concrete tile roof¹ on battens and counter-battens compared with the adjacent direct-nailed shingle roof. The heat transfer through the direct-nailed tile roof was 39% less than that through the ceiling of the asphalt shingle roof. They stated that the thermal mass of the concrete and the air space under the tile were reasons for the significant reduction in ceiling heat flows. Miller et al. (2005) and Miller (2006) found similar results for experiments on clay and concrete tile roofs and for field tests of stone-coated metal roofs.

Clay and Concrete Tile

Miller et al. (2005) observed that tiles with high profiles (S-mission) allowed the least amount of heat to penetrate into their respective roof decks (Figure 1). Venting occurred along the underside of the barrel of the S-mission tiles from soffitt to ridge. Of the S-mission roof tiles, the clay tile (SR54E90)² had the lowest heat flux crossing the deck; and subsequently, the heat penetrating the ceiling of the attic assembly was about 60% less than that entering through the ceiling of the attic assembly with asphalt shingles (Miller et al. 2005). The solar reflectance and thermal emittance of a slate concrete roof (SR13E83) and a medium-profile concrete tile (SR10E93) are very similar to that of the asphalt shingle (SR10E89), but the heat transfer through the roof and ceiling of the attic for the slate roof and the medium-profile tile roof were half that of the asphalt shingle roof. The reduction is due in part to the thermal mass of the tile and in part to buoyancy effects occurring in the inclined air channel that dissipates heat away from the deck.

Stone-Coated Metal

Miller, Wilson, and Karagiozis (2006) field tested stone-coated metal roofs on adjacent attic test assemblies very similar to the assemblies used for testing tile. A commercially available asphalt shingle with a solar reflectance of 0.093 and a thermal emittance of 0.89 (SR093E89) was selected as the control for comparing the thermal performance of the metal roof systems. A conventional dark-gray stone-coated metal shake (SR08E90) and a light-gray shake (SR26E90) were tested on identical batten and counter-batten constructions. All attic assemblies were equipped with 1 ft² of soffit and ridge

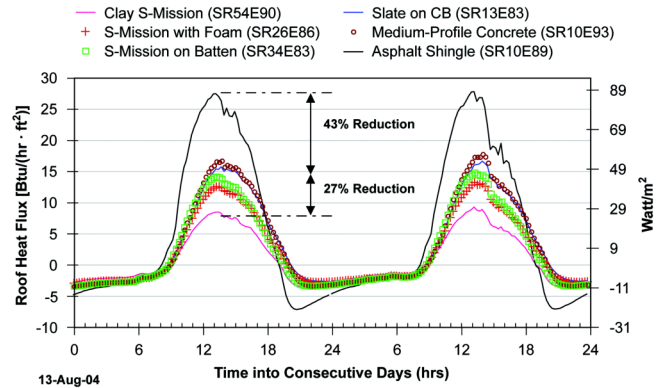


Figure 1 Heat penetrating clay and concrete tile roofs field tested on the steep-slope attic assembly at ORNL. Roof attachment: direct-nailed s-mission clay, direct nailed medium-profile concrete, spot-adhered foam s-mission concrete, batten and counter-batten flat concrete slate, batten s-mission and direct nailed asphalt shingle.

ventilation per 300 ft² of attic footprint for supporting attic ventilation.

Miller, Wilson, and Karagiozis (2006) observed that venting the underside of the dark-gray stone-coated metal shake significantly reduced the heat flow crossing the deck during solar noon (Figure 2). The dark-gray stone-coated metal shake and the asphalt shingle have almost identical reflectance and emittance characteristics, yet the heat flow crossing the roof deck of the dark-gray shake is just 70% of the heat flow crossing the roof deck of the asphalt control shingle. The 30% reduction in heat flow is due to ASV. Note that 2 in. (0.05 m) nominal dimension wood strips were nailed in the air space at the eave. The stricture did not seal the eave but is required by fire codes for California urban-wildland interface (UWI) areas.

Increasing solar reflectance from 0.08 to 0.26 caused the heat flow crossing the roof deck of the light-gray shake to be less than the heat flow crossing the roof deck of the dark-gray stone-coated shake. The reduction is about 15% of the heat crossing the deck of the control shingle roof (Figure 2). Miller, Wilson, and Karagiozis (2006) therefore concluded that ventilating the deck is just as important as is increasing solar reflectance and may be the stronger player in reducing heat gain into the attic. Note also that the heat flow due to ASV of the hotter dark-gray shake is more than double the amount of heat flow convected away from the deck of the light-gray shake. The hotter dark-gray shake causes greater buoyancy-induced airflows, and therefore ASV is somewhat self-regulating and offsets the effect of the darker, less reflective color. Also the stone-coated metal does not have the mass of a concrete tile, which further suggests that ASV has significant effects on the amount of heat penetrating the attic/roof plane.

1. Work conducted at Florida Solar Energy Center (FSEC). Terra cotta medium-profile concrete tile were field tested on FSEC's flexible roof test facility.
2. SRxx is the solar reflectance; "Eyy" defines the thermal emittance. Thus, labeling a white color as SR70E80 indicates that it has a solar reflectance of 0.70 and a thermal emittance of 0.80.

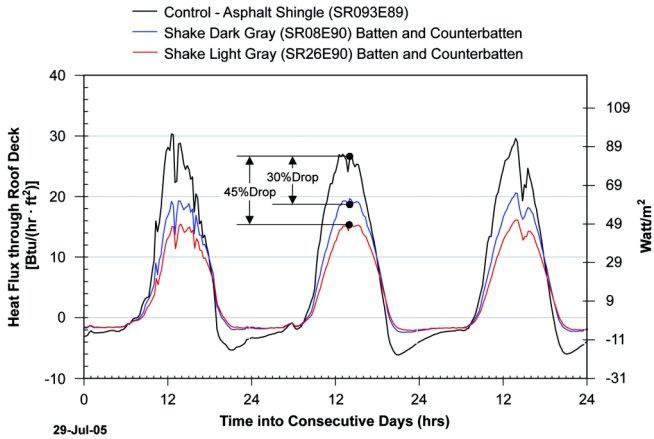


Figure 2 The effect of above-sheathing ventilation and solar reflectance for two stone-coated metal roofs compared with a direct-nailed shingle roof. Stone-coated metal installed on batten and counter-batten systems.

ABOVE-SHEATHING VENTILATION—ALGORITHM FORMULATION

The airflow in the inclined air space can be driven by both buoyancy and wind. The heat transfer due to the combination of these thermal and inertial forces is termed “mixed convection heat transfer” and, depending on the velocity of wind, the inertial forces can dominate the flow field. However, the International Wildland-Urban Interface Code³ (International Code Council 2006) requires the air space at the eave be closed⁴ for fire protection. In California UWI areas, roofs must be designed to resist burning embers landing on the structure and flame impingement (Quarles and Ten Wolde 2004). Therefore, the flow phenomenon will be one of natural rather than mixed convection because the fire code calls for 2 in. (0.05 m) nominal dimension lumber placed at the eave to restrict wind flows into the air space (Section 504.3). Blocking the eave also helps alleviate wind uplift on the offset-mounted roof. Hence, by fire code and wind design, the formulation of the algorithm is based solely on natural convection flow fields within the air space of the elevated roof system.

Measuring and correctly describing the natural convection airflow within the air space of an elevated roof cover is a key hurdle for predicting attic thermal performance. The airflow is laminar, and the heat transfer within the air space can

3. Section 504.2: “For roof coverings where the profile allows a space between the roof covering and the roof decking, the space at the eave ends shall be fire stopped to preclude entry of flames or embers.” Fire stopping can consist of 2-in. (0.05-m) nominal dimension lumber (Section 504.3).
4. Closing the eave does not imply it is sealed (airtight) because weep holes are required at the eave to permit the drainage of water from above the sheathing. Therefore, makeup air is available as buoyancy moves air up the roof’s inclination.

switch from conduction to single-cell convection to Bénard cell convection depending on the channel’s aspect ratio, the inclination, and the temperatures of the two parallel facing solid surfaces of the air space. The coexistence and competition of the various modes of heat transfer require experimental measurements and numerical simulations. Miller, Wilson, and Karagiozis (2006) and Miller et al. (2005) provided field data for stone-coated metal and tile roofs. This data was used to formulate and validate algorithms for predicting the airflow, temperature, and heat transfer occurring above the sheathing in the air space of the roof deck.

Estimates of the Natural Convection Flow Field

Temperature measures in the inclined air space of tile and stone-coated metal roofs show that the temperature in the air space is colder than the outdoor ambient air during late evening hours. As the morning sun heats the roof, airflows develop into boundary layer structures on each of the solid surfaces (Figure 3). The thermal resistance within each developing boundary layer behaves similarly to a single heated inclined plate facing upward, and boundary layer theory can provide estimates of the velocity and temperature field. The basic idea is to divide the natural convection flow into two sections. One is a free stream flow that is far enough away from the two parallel, inclined surfaces that it is inviscid. The second section is a very thin layer that is near the solid surfaces of the air space (sheathing and underside of the roof) where viscosity and thermal conductivity cause variations in velocity and heat transfer.

The bulk velocity and heat transfer coefficient in the air space were estimated by transforming the governing equations of continuity, motion, and energy into boundary layer form. The laminar boundary-layer equations in integral form for natural convection up an inclined surface are

Momentum:

$$\frac{d}{dx} \int_0^\delta u(u - u_\infty) dy + \frac{du_\infty}{dx} \int_0^\delta u dy = -v_\infty \frac{\partial u}{\partial y} \Big|_{y=0} \\ + \int_0^\delta g \beta (T - T_\infty) \sin(\theta) dy \quad (1)$$

Energy:

$$\frac{d}{dx} \int_0^\delta u(T - T_\infty) dy = -\alpha_{air} \frac{\partial T}{\partial y} \Big|_{y=0} \quad (2)$$

A third-order velocity profile and a second-order temperature profile were assumed with appropriate velocity and temperature boundary conditions for a constant flux (Burmeister 1983); these profiles become

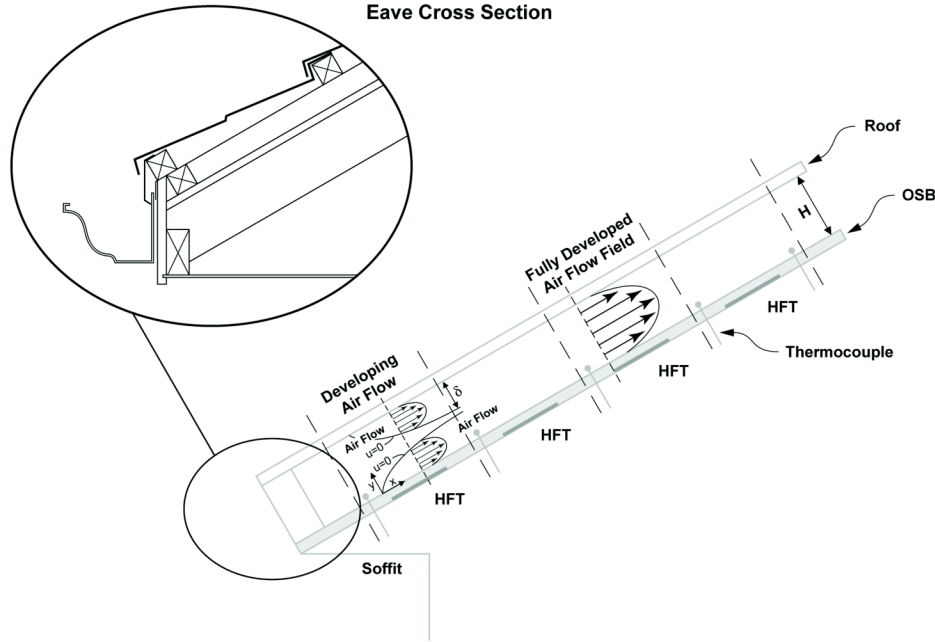


Figure 3 Entrance effects and establishment of fully developed flow fields in above-sheathing ventilation air space.

Velocity:

$$u(x,y) = A(x)\{\eta(1-\eta)^2\} \quad (3)$$

Temperature:

$$\frac{T(x,y) - T_\infty}{[(q'')\delta/2k_{air}]} = \{(-2\eta) + \eta^2\} \quad (4)$$

Substituting Equation 3 into Equation 1 and Equation 4 into Equation 2, and solving the coupled integral equations, leads to the following expression for the thickness of the boundary layer:

Boundary layer:

$$\delta = \frac{(288)^{1/5}}{(Pr)^{2/5}} \left[\frac{\{1 + 5/4Pr\}x}{\left\{ \frac{g\beta q'' \sin(\theta)}{v^2 k} \right\}} \right]^{1/5} \quad (5)$$

The balance of heat transfer at the solid wall by first principal equates conduction at the solid surface to convection within the boundary layer; it takes the form:

Heat balance:

$$-k_{air} \frac{\partial T}{\partial y} \Big|_{y=0} = \bar{h}_c \{T_{underside}(x, y=0) - T_\infty\} \quad (6)$$

Expressions for the temperature profile (Equation 4) and its derivative are evaluated at the wall and substituted into Equation 6 to derive the local Nusslet number (Bejan 1984):

Local Nusslet number:

$$Nu_x = \frac{2}{360^{1/5}} \left[\frac{\sin(\theta) Pr}{4/5 + Pr} \right]^{1/5} Ra_x^{1/5} \quad (7)$$

The bulk air velocity, the thickness of the boundary layer, and the local heat transfer coefficient were calculated using Equations 3, 5, and 7. Accordingly, the thickness of the boundary layer is about 0.91 in. (0.023 m) at a position 1 ft (0.30 m) up from the eave. It grows in thickness to about 1.73 in. (0.044 m) after 25 ft (7.62 m) of travel (Table 1). The bulk velocity is about 0.55 ft/s (0.168 m/s) after 10 ft (3.05 m) of travel, which reveals the difficulty in both the measurement and prediction of this airflow.⁵ The local heat transfer coefficient follows classical theory and drops steadily consistent with fully-developed heat transfer.

It is important to note that boundary layers are developing on both solid walls of the air space (Figure 3). The roof cover absorbs part of the solar irradiance while storing, convecting, reradiating, and conducting the remaining heat. The conducted heat sensed by the roof's underside is then convected to the air space. However, heat is also radiated across the air space to the sheathing, and part of the absorbed

⁵. Constant temperature “hot-wire” anemometers with 0–100 SCFM (0.047 m³/s) range are accurate to 1.5% of full scale, which implies a sensitivity threshold of 0.25 ft/s (0.076 m/s).

Table 1. Characteristic Local Thickness of a Boundary Layer¹ and the Bulk Velocity and Heat Transfer Coefficient Estimated within the Laminar Natural Convection Flow Traveling up an Inclined Surface

x-Distance from Eave, ft (m)	Boundary Layer Thickness, in. (mm)	Bulk Velocity, ft/s (m/s)	Local Heat Transfer Coefficient, Btu·h·ft ² ·°F (W/m ² ·K)
0.01(0.003)	0.36 (9.2)	0.03 (0.01)	1.052 (5.97)
0.5(0.152)	0.79 (20.1)	0.17 (0.05)	0.481 (2.73)
1(0.305)	0.91 (23.0)	0.22 (0.07)	0.419 (2.38)
10(3.048)	1.44 (36.5)	0.55 (0.17)	0.264 (1.50)
25(7.62)	1.73 (43.9)	0.79 (0.24)	0.220 (1.25)
100(30.48)	2.28 (57.9)	1.37 (0.42)	0.167 (0.95)

¹Field temperatures for stone-coated metal roofs measured around solar noon were used to calculate transport properties. Roof Slope was four-in-twelve (18.4°).

electromagnetic radiation is removed by convection to the air just above it. Beal and Chandra's (1995) counter-batten system elevated S-mission tile about 1½ in. (0.038 m) above the roof deck, yet boundary layers would easily have met within just ½ ft (0.15 m) of travel from the eave (Table 1). Also, a roof's aspect ratio for the air space (H/L) is large, and the velocity and temperature fields may become fully developed within a few feet of the eave.

Cadafalch et al. (2003) observed that the strength of the Rayleigh number (Ra number), the aspect ratio, the inclination angle, and surface radiation between the plates affected the free convection flow and heat transfer in large air channels. The Ra number incorporates the influence of the air's transport properties, the temperature gradient across the air space, and the geometry of the channel. The greater the Ra number, the greater is the buoyancy; and, in turn, the air velocity increases, causing possible transition from laminar to turbulent flow. The work of Mahajan and Gebhart as reported by Bejan (1984) showed that the transition from laminar to turbulent flow over flat plates occurs at a Grashof number ($Gr_L = Ra_L/Pr$) of about 10^9 , where the subscript (L) represents the length of a flat plate. However, because the roof's inclined air space has two merging boundary layers, transition is expected to occur at higher values of Gr_L . Summer field data for the stone-coated metal roofs revealed that Ra_L numbers ranged from 4×10^8 to a maximum of 3×10^{11} over the full length of the roof. Hence, for this roof application, flow in the channel was laminar with the exception of a probable transition to turbulence near the roof's ridge during periods of peak solar irradiance.

Clever, as reported by Hollands et al. (1976), was one of the first to demonstrate that for an inclined plate heated from below, the Nu number is a function of $Ra/\cos(\theta)$ rather than the Ra number and θ correlated separately. Clever's formulation requires the flow and temperature fields to be fully developed (i.e., invariant up the roof). Given that the height of the air space in practice can be 3/8 to 1½ in. (0.0095 to 0.038 m) and the roof length is 30 ft (9.1 m), the aspect ratio H/L is large, exceeding 240; and we estimate using laminar duct flow theory⁶ (Brumeister 1983) that entrance region effects settle out at least within 10 ft (3.05 m) of the eave. Therefore, heating

from the solid surfaces occupies the entire air gap easily within 1 ft (0.30 m) of travel and is estimated to be fully developed after 10 ft (3.05 m) of travel from the eave (Figure 3). Further analysis requires computer modeling to assist with the prediction of airflow and local heat transfer.

Computational Fluid Mechanics

A computational fluid dynamics code (CFD) simulated the two-dimensional steady-state channel flow between two parallel plates. The x-momentum, y-momentum, and energy equations were discretized and solved numerically subject to uniform wall temperatures that were set to measurements collected for the dark gray stone-coated metal roof (SR08E90) tested on the Envelope Systems Research Apparatus (Figure 2 and Table 2). For summer conditions, the top surface was always held at a higher temperature than the bottom surface to simulate the heat transfer observed in Figure 2. For winter, the sheathing was set at a higher temperature than the roof's underside. Here, the temperature of air within the air space is less than the outdoor ambient air temperature, and flow moves down the roof's sheathing toward the eave. Conditions of no-slip at the wall and an impermeable wall were used in the solution procedure. Roof pitches of 1-in-12, 2-in-12, 4-in-12, and 8-in-12 were investigated to better understand the strength of natural convection forces occurring within the inclined air space heated from above and from below.

An approach was formulated to correlate and predict the natural convection airflow and heat transfer in the air space given the outdoor ambient air temperature and the bulk air temperatures in the air space. A number Ra_H^* was defined as $Ra_H \{ \sin(\theta) \}$:

Ra_H^* number:

$$Ra_H^* = \frac{g\beta \sin(\theta) \{\bar{T}_{airspace} - T_{ODAir}\} H^3}{v\alpha} \quad (8)$$

where the bulk temperature in the air space is calculated using the following simple expression:

⁶ Fully developed laminar duct flow $L/H \approx 0.05 \cdot RePr$.

Table 2. Temperature Boundary Conditions Used in CFD Simulations

	Daytime		Nighttime	
	Max, °F	Min, °F	Max, °F	Min, °F
January field measures for dark gray stone-coated metal roof (SR08E90)				
Outdoor air	50.6	13.5	49.7	13.6
Underside of metal roof	111.0	2.2	49.2	0.7
OSB deck	80.7	10.0	54.0	9.9
July field measures for dark gray stone-coated metal roof (SR08E90)				
Outdoor air	92.6	69.5	89.9	68.1
Underside of metal roof	171.1	70.4	129.3	61.5
OSB deck	136.6	69.7	118.3	67.5
Conversions: °C = (°F-32.0)/1.8				

Bulk air temperature:

$$\bar{T}_{airspace} = (T_{underside} + T_{sheathing})/2$$

Field data for the stone-coated metal roofs showed that the bulk air temperature in the air space tracked very well the average temperature of the two solid surfaces (Figure 4). The field temperatures were measured 8 ft (2.4 m) from the eave using Type-T copper constantan thermocouples taped to the stone-coated metal roof ($T_{underside}$), placed in the free stream of the air space, and taped to the sheathing of the roof deck ($T_{sheathing}$). The (x) symbols in Figure 4 represent the average temperature of the roof underside and sheathing, while the solid pink line is the measured free stream bulk temperature, again measured 8 ft (2.4 m) from the eave (Figure 4). The field data help confirm that the heating effect of the roof has fully bridged across the air space and that the flow and temperature fields are close, if not fully developed.

CFD simulations yielded Ra_H^* numbers ranging from about 1500 during mild summer evenings to a high of 18,000 during periods of peak irradiance. Numerical solutions for the velocity field were reduced to mass flow rate and Re number,⁷ which was correlated as a dependent variable of the reduced independent parameter Ra_H^* number (Figure 5). The symbols in Figure 5 represent reduced CFD simulation data that are labeled consistently with the temperatures used for the solid surface boundary conditions (Table 2). As an example, the green squares represent CFD results of $Re = f\{Ra_H^*\}$ for the daytime minimum and nighttime minimum measures (Table 2) during July field tests.

The correlation for Re number has an average absolute error within 5% of the CFD Re data, and the correlation's root-mean square error⁸ is ≈ 0.99 . Regression analysis included inclinations of $9^\circ < \theta < 34^\circ$. Kimura et al. (2002) showed tran-

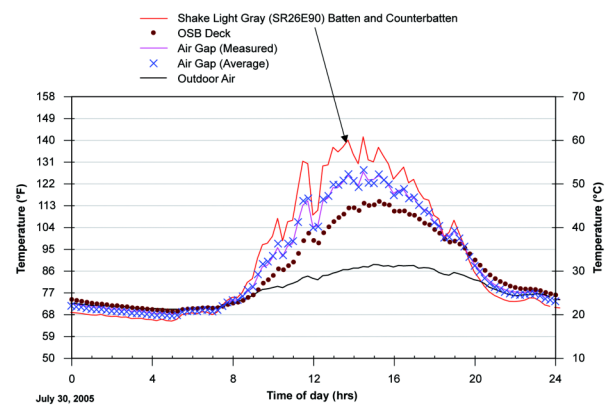


Figure 4 Field measures of the stone-coated metal roof and air space temperatures showing comparison of measured and derived bulk air temperature in the air space.

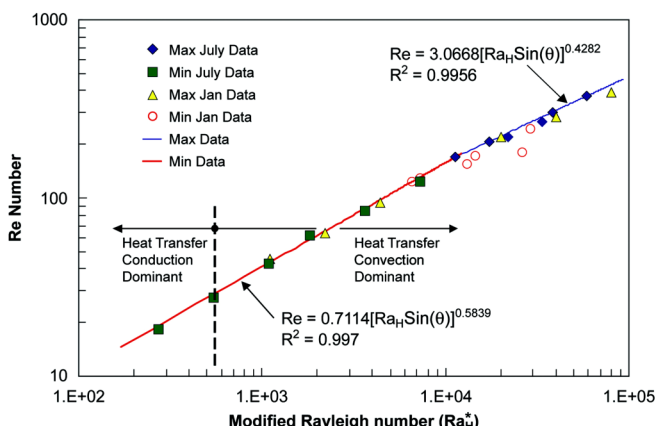


Figure 5 Reynolds number predictions using modified Ra_H^* number from CFD modeling for inclinations of (2/12, 4/12 and 8/12).

⁷. Re number defined as $Re = \frac{\rho \bar{u} H}{\mu}$.

⁸. Root-mean square (RMS) error describes the differences between Re numbers predicted by the correlation and Re values reduced from CFD simulations.

sitional turbulent flows at Ra_x of 10^7 for plates inclined 15° . Figure 5 shows two distinct regions with possible transition to turbulence occurring at about Ra_H^* of 10,000 (i.e., $Ra_L \approx 10^6$); therefore, we formulated $Re = f\{Ra_H^*\}$ by

$$Ra_H^* \text{ number} \leq 10,000$$

$$Re = 0.7114 \left[Ra_H^* \right]^{0.5839} \quad (9)$$

$$Ra_H^* \text{ number} > 10,000$$

$$Re = 3.0668 \left[Ra_H^* \right]^{0.4282} \quad (10)$$

Hollands et al. (1976) observed that the heat transfer across an inclined air space can switch from conduction to single-cell convection to Bénard cell convection depending on the magnitude of Ra_H . For Ra_H numbers of less than $1708/\cos(\theta)$, Hollands observed no naturally induced airflow within the cavity, and heat transfer across the air space occurs exclusively by conduction. For the CFD results displayed in Figure 5, conduction-dominated heat transfer occurs for $Ra_H^* \leq 570$; however, airflow occurs as buoyancy forces overcome viscous forces, and the heat transfer within the channel is dominated by convection for $Ra_H^* > 570$.

ATTICSIM COMPUTER TOOL

An *a priori* knowledge of the airflow within the air space is key to determining the portion of heat penetrating the roof deck and that convected away through the ridge vent. Given the airflow, energy balances can be derived for the external and internal surfaces of the roof and attic and solved using open literature computer tools for predicting thermal performance.

Wilkes (1991) formulated and validated an attic simulation tool titled “AtticSim.” Wilkes also published the tool as an ASTM standard (ASTM 2004) for estimating the heat transfer through ceilings under attics containing radiant barriers. The ability to simulate ASV was implemented into AtticSim because (1) the source code is readily available in the open literature and (2) the code can simulate a full year of data (8760 bin hours) and solve for the diurnal heat flows in less than 5 min on a 1.6 GHz processor. The model can account for different insulation R-values and/or radiant barriers attached to the various attic surfaces. It also has an algorithm for predicting the effect of air-conditioning ducts placed in the attic as reported by Petrie et al. (2004) and described in ASTM C 1340 (2004). Salient features of AtticSim (including the source code) are provided by Wilkes (1991).

The code uses heat balances to mathematically describe the conduction at the interior (facing the attic) and the exterior of the two gables, the two eaves, the two roof decks, and the ceiling; the convection at the exterior and interior surfaces; the radiant heat exchange between surfaces within the attic enclosure; the heat transfer to the ventilation air stream; and the latent heat effects due to sorption and desorption of moisture at

the wood surfaces. Conduction heat transfer through the roof decks, gables, and vertical eaves is modeled using the thermal response factor technique (Kusuda 1969), which requires the thermal conductivity, specific heat, density, and thickness of each attic section. The energy balances at the interior surfaces (facing the attic space) and the exterior surfaces comprise 14 algebraic equations. An additional energy balance is used to calculate the attic air temperature given an iterative solution of the 15 simultaneous equations yields the interior and exterior surface temperatures and the attic air temperature at 1-hour time steps. The heat flows at the attic’s ceiling, roof sections, gables, and eaves are then calculated using the conduction transfer function equations. Petrie (2004) and Miller et al. (2004) provide validation of the code’s ability to predict attic ventilation for soffit and ridge venting. The tool was validated by Wilkes (ASTM 2004) against summer field experiments and is capable of predicting the ceiling heat flows integrated over time to within 5 to 10% of the field measurement for attics without radiant barriers. Wilkes (1991) conducted validations for attics having direct-nailed roof products. Miller et al. (2004) also validated AtticSim against a steep-slope attic assembly having direct-nailed asphalt shingles (SR093E89). The model predicted the surface temperature of the shingles, the attic air temperature, and, as a result, the heat flow penetrating the conditioned space within 5% of field measures. Until now, it had not been used to predict the effects of ASV prevalent in tile and stone-coated metal roofs.

AtticSim Algorithm

AtticSim’s input specifications were modified to include two additional roof surfaces (shaded rows in Table 3) that are elevated above the roof deck; the amount of elevation above the deck is specified in an input block data file. Logical variables were also added to the block data file for directing the code to solve either the case of a direct-nailed roof assembly (default case) or the new case for ASV. Herein is the correlation discussed earlier for natural convection flows.

The added roof cover forms an inclined channel that senses both convection and radiation with the parallel solid surfaces of the roof deck and the roof cover. An energy balance on a differential section of the air space yields

ASV energy balance:

$$(mC_p)_{air} \bar{T}_{air \text{ at } x} + (q''_{roof_{underside}})(\Delta x)(W) = \\ (mC_p)_{air} \bar{T}_{air \text{ at } x + \Delta x} = (q''_{roof_{deck}})(\Delta x)(W) \quad (11)$$

Normalizing x as $\bar{x} = x/L$ and substituting convective terms for the fluxes at the solid surfaces leads to the ordinary non-homogenous differential equation (ODE) for the bulk air temperature:

Table 3. Sequence of Surfaces Input to AtticSim for Modeling Attic

Surface Index	Descriptors ¹ for Interior and Exterior Surfaces
1	Attic floor
2	East facing roof or roof deck ²
3	West facing roof or roof deck ²
4	South facing gable
5	North facing gable
6	East facing eave wall
7	West facing eave wall
8	East facing elevated roof
9	West facing elevated roof

¹Orientation assumed for a north-south ridge.

²Roof deck for ASV case includes tar paper, oriented strand board panels, and roof joists.

ODE:

$$\frac{d\bar{T}_{air}}{d\bar{x}} + \frac{W(L)}{(mC_P)_{air}} [\bar{h}c_{underside} + \bar{h}c_{deck}] \bar{T}_{air} = \frac{W(L)}{(mC_P)_{air}} \quad (12)$$

$$[TIS_{(i=8,9)} \bar{h}c_{underside} + TOS_{(i=2,3)} \bar{h}c_{deck}]$$

Solution of the ODE yields the bulk air temperature as a function of its displacement (\bar{x}) up the roof as

Bulk temperature:

$$\bar{T}_{air}(\bar{x}) = \frac{b}{a}(1 - e^{-a\bar{x}}) + (T_{ODair})e^{-a\bar{x}} \quad (13)$$

Using the boundary conditions $\bar{T}_{air}(\bar{x}=0) = T_{ODair}$ and $\bar{T}_{air}(\bar{x}=1) = \frac{b}{a}(1 - e^{-a}) + T_{ODair}e^{-a}$ leads to the average bulk temperature over the east ($i=8$) and west ($i=9$) oriented roof sections as follows:

Bulk average:

$$\bar{T}_{air} = \frac{b}{a} \left(1 + \frac{(e^{-a} - 1)}{a} \right) - T_{ODair} \left[\frac{(e^{-a} - 1)}{a} \right] \quad (14)$$

where

$$a = \frac{(A * \bar{h}c)_{(i=8,9)} + (A * \bar{h}c)_{(i=2,3)}}{(mC_P)_{air}}$$

$$b = \frac{(A * \bar{h}c * TIS)_{(i=8,9)} + (A * \bar{h}c * TOS)_{(i=2,3)}}{(mC_P)_{air}}$$

Equation 14 was coded into AtticSim for the bulk air temperature averaged over the length of the roof; however, the equation needs the exterior temperatures of the roof deck ($TOS_{(i=2 \text{ and } 3)}$) and the interior temperatures of the elevated roofs ($TIS_{(i=8 \text{ and } 9)}$) as well as expressions for the convective heat transfer coefficients. The surface temperatures are derived from expressions for the conduction response factor equations and expressions for the various heat transfer mechanisms acting on the respective surfaces.

Energy balances at the interior of the elevated roof ($i=8$ and 9 , shaded rows in Table 3) balance thermal storage to the heat conducted through to the air space, the heat convected to the air, and the heat radiated across the air space to the roof deck by

Interior surface:

$$\begin{aligned} & \sum_{j=0}^N Z_{(i,j)} \{ TIS_{(i,j)} - T_{Ref} \} - \sum_{j=0}^N Y_{(i,j)} \{ TOS_{(i,j)} - T_{Ref} \} \\ & + CR_{(i)} QI'_{(i)} + \frac{b_{(i)}}{2} \sum_{j=0}^N Z_{(i,j)} \{ TIS_{(i,j)} - T_{Ref} \}^2 - \frac{b_{(i)}}{2} \\ & \times \sum_{j=0}^N Y_{(i,j)} \{ TOS_{(i,j)} - T_{Ref} \}^2 + \bar{h}_{c(i)} \{ TIS_{(i,0)} - \bar{T}_{airspace} \} \quad (15) \\ & + \sum_{\substack{i=8, k=2 \\ \text{or} \\ i=9, k=3}} \frac{\sigma \{ TIS_{(i,0)}^4 - TOS_{(k,0)}^4 \}}{\left\{ \frac{1-\varepsilon_i}{\varepsilon_i} + \left(\frac{1-\varepsilon_k}{\varepsilon_k} \right) A_i + \frac{1}{F_{i-k}} \right\}} - h_{fg} \dot{m}_{water(i)} = 0 \end{aligned}$$

Similar balances for the exterior surfaces ($i=8$ and 9 , shaded rows in Table 3) equate the absorbed solar irradiance to conduction, radiation, thermal storage and convection by

Exterior surface:

$$\begin{aligned} & \sum_{j=0}^N Y_{(i,j)} \{ TIS_{(i,j)} - T_{Ref} \} - \sum_{j=0}^N X_{(i,j)} \{ TOS_{i,j} - T_{Ref} \} \\ & + CR_{(i)} QO'_{(i)} + \frac{b_{(i)}}{2} \sum_{j=0}^N Y_{(i,j)} \{ TIS_{(i,j)} - T_{Ref} \}^2 - \frac{b_{(i)}}{2} \quad (16) \\ & \times \sum_{j=0}^N X_{(i,j)} \{ TOS_{(i,j)} - T_{Ref} \}^2 + \bar{h}_{c(i)} \{ T_{ODAir} - TOS_{(i,0)} \} \\ & + \varepsilon_{(i)} \sigma \{ T_{Sky} - TOS_{(i,0)} \} + (1 - \rho)_{(i)} I_{Solar(i)} = 0 \end{aligned}$$

Further details showing the derivation of the response factors are presented in ASTM C 1340 (2004). Suffice it to say these

response factor equations relate the present and previous temperatures of the interior and exterior surfaces. The index “i” refers to the respective surface (Table 3 shaded rows only for ASV) for which the heat balance is written. The “j” index represents the time sequence for the conduction transfer function, with $j = 0$ representing the current time. The mathematical descriptive for ASV adds an additional six equations to be solved, resulting in a total of 21 equations expressing the interior and exterior temperatures of the roof and attic assembly (Table 3), the ventilation air of the attic, and the two ASV airflows of the elevated roofs.

Gauss-Jordan elimination was used to iteratively solve for the temperatures and airflow rates. The system of equations is arranged into a matrix with the interior and exterior surface temperatures and air temperatures at the current time step being the unknown quantities, matrix array $[T]$. Values for these temperatures at previous time steps are known and are included in a source term named $[BB]$. The matrix equation $[AA][T]=[BB]$ is solved for the $[T]$ array of surface and air temperatures. The surface temperatures are then used to calculate the heat flows at all attic surfaces (Table 3) using the conduction transfer function equations (Wilkes 1991):

Interior surface:

$$QI = \sum_{j=0}^N Z_{(j)} \{ TIS_{(j)} - T_{Ref} \} - \sum_{j=0}^N Y_{(j)} \\ \{ TOS_{(j)} - T_{Ref} \} + CR * QI' + \frac{b}{2} \sum_{j=0}^N Z_{(j)} \quad (17)$$

$$\{ TIS_{(j)} - T_{Ref} \}^2 - \frac{b}{2} \sum_{j=0}^N Y_{(j)} \{ TOS_{(j)} - T_{Ref} \}^2$$

Exterior surface:

$$QO = \sum_{j=0}^N Y_{(j)} \{ TIS_{(j)} - T_{Ref} \} - \sum_{j=0}^N X_{(j)} \\ \{ TOS_{(j)} - T_{Ref} \} + CR * QO' + \frac{b}{2} \sum_{j=0}^N Y_{(j)} \quad (18)$$

$$\{ TIS_{(j)} - T_{Ref} \}^2 - \frac{b}{2} \sum_{j=0}^N X_{(j)} \{ TOS_{(j)} - T_{Ref} \}^2$$

CONVECTIVE COEFFICIENTS IN THE INCLINED AIR SPACE

Understanding the regime of heat transfer within the air space for ASV is also required for accurately modeling the overall heat transmission through the elevated roof assembly. Elenbaas (1942) studied the heat dissipation between parallel isothermal plates fixed at the same temperature. Hollands et al. (1976); Arnold, Catton, and Edwards (1976); and, most recently, Brinkworth (2000) studied natural convection heat transfer observed below flat-plate photovoltaic cladding.

During winter exposure, the warmer roof deck is positioned below the cooler roof cover, much as in the problem studied by Hollands et al. (1976). Here, a denser air layer near the roof's underside overlies lighter air adjacent to the roof deck. Hollands observed that the heat transfer across the air channel can switch from conduction to single-cell convection to Bénard cell convection depending on the magnitude of the Ra_H number. For Ra_H numbers of less than $1708/\cos(\theta)$, there is no naturally induced airflow within the cavity, and the heat transfer occurs exclusively by conduction. However, as the flow increases as a result of buoyancy, the heat transfer within the channel can switch to Bénard cell convection, which has hexagonal cells with flow ascending in the center and descending along the sides of the air channel.

Convective heat transfer from the air space when the roof deck was warmer than the roof cover was calculated using Hollands correlation:

Nu number:

$$\frac{\bar{h}cH}{k_{air}} = 1 + 1.44 \left[1 - \frac{1708}{Ra_H \cos(\theta)} \right]^* \\ \left(1 - \frac{1708[\sin(1.8\theta)]^{1.6}}{Ra_H \cos(\theta)} \right) + \left[\left(\frac{Ra_H \cos(\theta)}{5830} \right)^{1/3} - 1 \right]^* \quad (19)$$

where the $[]^*$ designates $[X]^* = 0.5 [X] + X$.

Holland recommends Equation 19 for free convection heat exchange through an air space having an inclination of $0 \leq \theta \leq 60^\circ$ and $0 < Ra_H < 10^5$.

During summer exposure, the roof cover is hotter than the roof deck, and Bénard cell convection does not occur within the air space because the lighter air layer is above the denser air layer. Brinkworth (2000) studied this situation as applied to natural convection flows under flat-plate photovoltaic cladding. His study was conducted for inclinations of 30, 45, 60, and 90°. He observed that for long and narrow ducts, forced convection expressions can be successfully used even in buoyancy-driven flows. Brinkworth's correlation was used for the case in which the roof is warmer than the deck; it applies to laminar parallel plate flow (no wind effects) having a uniform heat flux (sun) incident on the hotter plate.

Nu number:

$$\frac{\bar{h}c(D)}{k_{air}} = 5.385 + \frac{0.071}{\left(\frac{L}{DR_D} + 0.002 \right)} \quad (20)$$

Air properties are evaluated at the film temperature, which is the average of the surface and air temperatures, to account for the temperature dependence of the properties.

VALIDATION OF ASV ALGORITHM

AtticSim was compared with field tests conducted during July 2005 on a conventional dark gray stone-coated metal

shake (SR08E90) and a light-gray infrared reflective shake roof (SR26E90), as discussed in the section “Above-Sheathing Ventilation Field Data.” These roofs were offset from the roof deck by about $\frac{3}{4}$ in. (0.019 m) using a batten and counter-batten system. Temperatures are compared in Figure 6 for several of the attic and roof surfaces and in Figure 7 for measured and calculated attic air temperatures. Results (Figure 6) show that the conduction transfer equations are accurately predicting the temperature on the underside of the metal roof (SR26E90), the deck sheathing temperature facing the roof, the deck temperature facing the attic, and the attic floor temperature. The code slightly overpredicts field measurements during periods of peak irradiance and slightly underpredicts field temperatures during late night hours (Figure 6). However, the differences are consistent. An overprediction of the roof’s underside temperature is carried through all the way to the attic floor, where the results show that the code also overpredicts the temperature of the attic floor (Figure 6). The average absolute error between Attic-Sim’s predictions and measured field data was no worse than 6% of field measures for the full week of July data (Table 4).

The trend for attic air temperatures was similar to that observed for the temperatures of the various surfaces (Figure 7). There is a slight overprediction at solar noon, followed by underprediction for night-time measurements. The average absolute error is of the same order: about 6%. The code accurately predicts the bulk air temperature within the air space of the ASV cavity. For the week of data, the average absolute error was less than 1% of measurements acquired from thermocouples placed in the air space of the stone-coated roof (SR26E90). The prediction is based on the formulation of Equation 14, which accounts for the mass flow rate of the ASV, and on the convective heat transfer coefficients used to

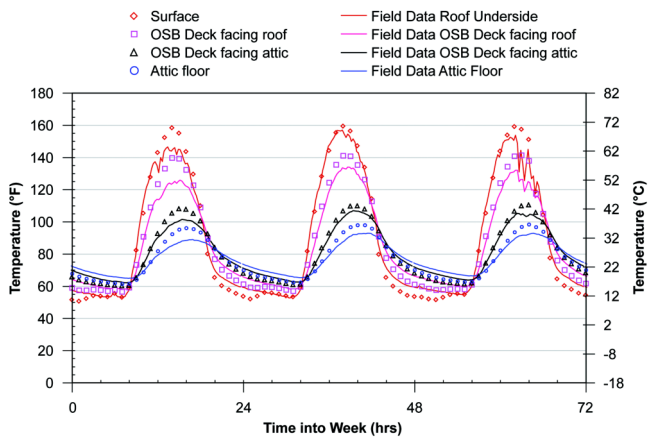


Figure 6 AtticSim model (open symbols) estimation of attic surface temperatures as compared to field measures (solid lines) acquired for the stone-coated metal roof (SR26E90) tested in July 2005.

describe heat transfer from the solid surfaces of the inclined channel and the air space. Therefore, we conclude that the algorithm for airflow, Equations 9 and 10, and the correlations by Brinkworth (2000) and by Hollands et al. (1976) are capturing the heat transfer physics of the natural convection flow quite well.

Miller, Wilson, and Karagiozis (2006) embedded a heat flux transducer (HFT) in the roof to measure the flux conducted to the underside of the deck (facing the attic). Attic-Sim predicts the flow of heat at the internal and external surfaces of an attic using Equations 17 and 18. The prediction and measured heat flow agreed well to within 15% of the cumulative heat flow crossing the roof deck during the full week of July 2005 exposure (Figure 8). The code appears to overpredict deck heat flows during the late evening hours, when the air temperature gradient from the attic air to the outdoor air is at its lowest value. The heat fluxes across the air space (simulated by the model) are also shown in Figure 8. The blue line represents heat flow at the underside of the stone-coated metal roof (SR26E90), and the black dashed line is the heat flow entering the top of the roof deck at the sheathing (Figure 8). The difference in these values multiplied by the surface area of the deck is the heat dissipated through the ridge vent by ASV. As expected, ASV provides the most benefit during periods of peak irradiance (Figure 8). For example, the stone-coated metal roof incurred a flux of about 30 Btu/h·ft² (94.6 W/m²) entering the air space, while 25 Btu/h·ft² (78.8 W/m²) crossed over to the roof deck (see Figure 8, 24-h through 48-h time period). The 16% reduction in heat flux is carried away by ASV. The heat flux convected to the air space is converted to a rate and is shown in Figure 9 compared with the same value calculated by an energy balance on the ventilated air space. The energy balance is as follows:

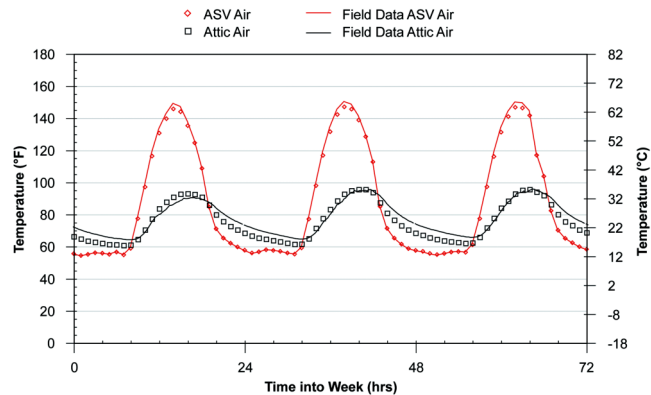


Figure 7 AtticSim model (open symbols) estimation of attic air temperatures and above-sheathing ventilation (ASV) air temperatures as compared to field measures (solid lines) acquired for the stone-coated metal roof (SR26E90) tested in July 2005.

Table 4. Average Absolute Errors (AAE) between Field Measures for Stone-Coated Metal Roof (SR26E90) and AtticSim's Predictions Shown in Figures 6 and 7

Measurement Point	Roof Underside	Deck-Facing Roof	Deck-Facing Attic	Attic Floor	ASV Air Space	Attic Air
AAE	3.8%	5.6%	5.3%	5.6%	0.86%	6.0%

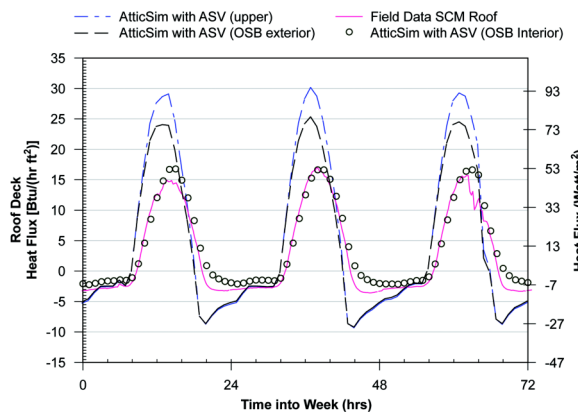


Figure 8 Validation of AtticSim's ability to predict the measured heat flux penetrating through the OSB roof deck.

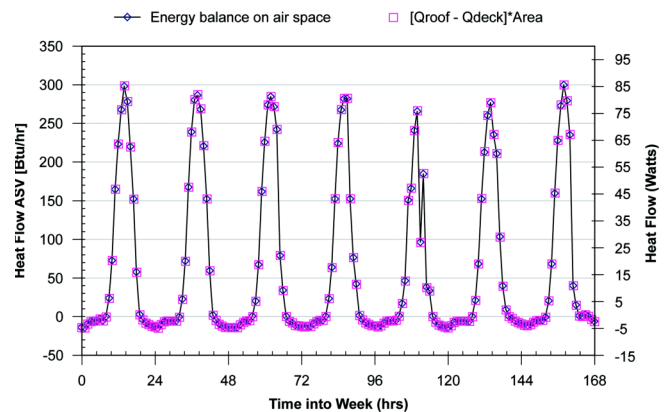


Figure 9 Heat flows exiting the ridge vent for above-sheathing ventilation calculated by two different approaches to check consistency of the algorithm.

ASV heat flow:

$$Q_{ASV} = (mC_P)_{air}\{\bar{T}_{\bar{x}} = 1 - T_{\bar{x} = 0}\} \quad (21)$$

where the mass flow rate in the air space is derived from our correlation Equations 9 and 10, and the bulk air temperature is computed by Equation 14. The two different approaches calculate the rate of heat dissipated by ASV, and both approaches should and do yield the same result, confirming the calculation consistency of the procedure.

Another check was made to test the consistency of the procedure for obtaining the mass flow rate of air in the air space (Figure 10). We used the field data for July 2005, implemented the algorithm into a spreadsheet, and hand-calculated the mass flow rate based on field-measured temperatures. Results showed the algorithm in AtticSim calculated the results from the spreadsheet very well (Figure 10), again validating the consistency of the procedure. Miller (2006) also designed a procedure to measure the airflow using tracer gas techniques outlined in ASTM E 741 (ASTM 2000) and by Lagus et al. (1988). The procedure required monitoring the decay rate of the tracer gas CO₂ over time using the following equation, derived from a continuity balance for the concentration of CO₂:

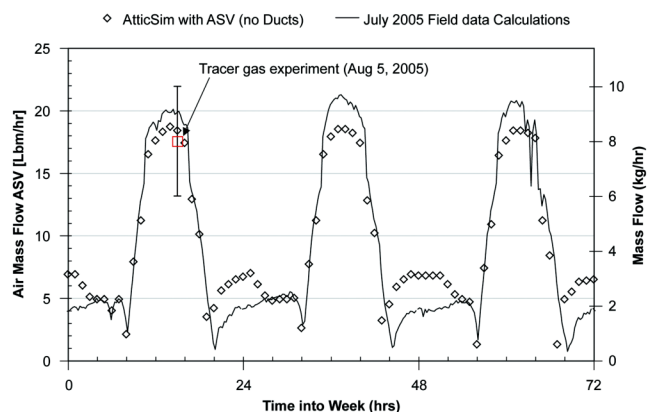


Figure 10 Mass flow rates in the above-sheathing ventilation air space calculated by AtticSim, verified by field measurements reduced by spreadsheet calculations and validated by tracer gas experiments conducted in roof deck.

Volumetric flow rate:

$$\dot{V}_{Air} = -\frac{VOL_{Channel}}{t} \ln \left[\frac{C(t) - C_{\infty}}{C_{ini} - C_{\infty}} \right] \quad (22)$$

Miller (2006) derived a reduced bulk air velocity of about 0.26 ft/s (0.079 m/s) from the procedure, which yielded a volumetric flow rate of about 18 cfm (0.0085 m³/s) ±25%. Therefore, the airflows shown in Figure 10 are within tolerance of

data reduced from tracer gas measurements (although not from the same exact time), providing further validation of the code.

CONCLUSIONS

The collection of experimental data (pre- and post- ASV) for tile and stone-coated metal roofs and the coincident formulation of a computer model was benchmarked against these data. The new development expands AtticSim for solving the case of ASV commonly used in clay and concrete tile roofs and stone-coated metal roofs. The subsequent heating of the air formed between the waterproofing layer and the sheathing produces complex thermally induced air flow patterns and significantly reduces the heat flow penetrating into the attic by at least 30% of the flows observed for a direct-nailed roof. AtticSim provided accurate predictions (within $\pm 5\%$ of field measures) for surface temperatures and integrated ceiling and deck heat fluxes (within $\pm 10\%$ of field measures) when exercised for the case of ASV.

Computational fluid modeling led to the development of a correlation for quickly estimating the naturally induced air flow within the ventilated air space. The correlation accounts for the geometry and roof slope and provides quick and accurate measures of the airflow. Successful correlation of this natural convection flow phenomenon was key to solving for the heat flows crossing the air space. The correlation does not take into account the effect of a forced flow component, which may aid or oppose the naturally induced flow, nor the air leakage between clay or concrete tile overlaps.

RECOMMENDATIONS

A priori understanding of the optimal air gap (aspect ratio) would directly assist with the development of standards for offset mounting of tile, metal, and asphalt shingle roofs. The code would greatly help in development of these standards. The computer model should also be used to evaluate the potential energy savings in a variety of climates to determine whether, in light of the estimated system cost, further product development efforts are justified. This early focus on economics will also help the industry ensure that target market needs are met.

NOMENCLATURE

x	= Dimension from eave to ridge
y	= Dimension normal to roof inclination
L	= Length of roof eave to ridge
H	= Height of air space
W	= Width of roof gable to gable
A	= Area (cross-sectional or plane)
P	= Wetted perimeter of inclined channel
D	= Hydraulic diameter = $4A/P$

⁹. The uncertainty of measurement for the tracer gas technique was calculated on the basis of a first-order error analysis and is estimated at about $\pm 25\%$ of measurement.

θ	= Inclination of roof
$u(x, y)$	= x -component of velocity
$v(x, y)$	= y -component of velocity
δ	= Boundary layer thickness
T	= Temperature
h_c	= Convective heat transfer coefficient
Nu_x	= Local Nusselt number

Air Properties

ν	= Kinematic viscosity
k	= Thermal conductivity
ρ	= Density
μ	= Dynamic viscosity
C_p	= Specific heat
β	= Coefficient thermal expansion
α	= Thermal diffusivity
h_{fg}	= Latent heat of vaporization

Roof Surface Properties

SR	= Solar reflectance
TE	= Thermal emittance
I	= Solar irradiance
\dot{m}	= Mass flow rate in air space
q''	= Heat flux
C	= Concentration of CO_2

Scaled Parameters

\bar{x}	= x/L
η	= y/δ
\bar{u}	= Average velocity in air space
\bar{T}	= Bulk temperature in air space
Re	= Reynolds number = $\rho \bar{u} H / \mu$
Re_D	= Reynolds number based on D
Ra_H	= Rayleigh number based on H
Ra_L	= Rayleigh number based on L
Pr	= Prandtl number = ν / α
Gr_L	= Grashof number = Ra_L / Pr
$A\{x\}$	= $\frac{g\beta\{T(x) - T_\infty\}\delta^2 \sin(\theta)}{4\nu}$
$A\{x\}^{10}$	= $\frac{g\beta\{q''\}}{4\nu} \left[\frac{\delta}{2k} \right] \delta^3 \sin(\theta)$
σ	= Stefan-Boltzmann constant

Conduction Response Factor Terms (Wilkes 1991)

TIS	= Temperature of surface facing attic
TOS	= Exterior temperature of attic surface

¹⁰. Assumes constant flux boundary condition.

T_{ref}	= Reference temperature
Q_I	= Heat flux at inside surface of attic at present time (positive heat flow is from inside attic to outside attic)
Q_O	= Heat flux at outside surface at present time
Q'_I	= Heat flux at inside surface of attic at previous time
Q'_O	= Heat flux at outside surface at previous time
$b(i)$	= Parameter for temperature dependence of thermal properties
$X(i,j)$	= Conduction transfer function for surface i and time steps $j = 0-N$
$Y(i,j)$	= Conduction transfer function for surface i and time steps $j = 0-N$
$Z(i,j)$	= Conduction transfer function for surface i and time steps $j = 0-N$
CR	= Ratio of two consecutive response factors termed the common ratio

Subscripts

i	= Index for attic surfaces (Table 3)
j	= Time sequence ($j=0$ is present time)
∞	= Free stream

REFERENCES

- Arnold, J.N., I. Catton, and D.K. Edwards. 1976. Experimental investigation of natural convection in inclined rectangular regions of differing aspect ratios. *Journal of Heat Transfer* February: 67–71.
- ASTM. 2000. *ASTM Standard E741-00, Standard Test Method for Determining Air Change in a Single Zone by Means of a Tracer Gas Dilution*. West Conshohocken: American Society for Testing and Materials.
- ASTM. 2004. *ASTM Standard C 1340-04, Standard Practice for Estimation of Heat Gain or Loss Through Ceilings Under Attics Containing Radiant Barriers by Use of a Computer Program*. West Conshohocken: American Society for Testing and Materials.
- Baker, M. C. 1980. *Roofs*. Montreal, Quebec, Canada: Polyscience Publications.
- Beal, D. and S. Chandra. 1995. The measured summer performance of tile roof systems and attic ventilation strategies in hot humid climates. *Thermal Performance of the Exterior Envelopes of Buildings VI*. December 4-8 Clearwater, Florida.
- Bejan A. 1984. *Convection Heat Transfer*. New York: John Wiley & Sons.
- Brinkworth, B.J. 2000. A procedure for the routine calculation of laminar free and mixed convection in inclined ducts. *International Journal of Heat and Fluid Flow*. 21:456–462.
- Burmeister, L. 1983. *Convective Heat Transfer*. New York: John Wiley & Sons.
- Cadafalch, J., A. Oliva, G. Graaf, and X. Albets. 2003. Natural convection in a large, inclined channel with asymmetric heating and surface radiation. *ASME Transactions* 125. October: 812–820.
- Elenbaas, W. 1942. Heat dissipation of parallel plates by free convection. *Phsica* 9(1):2–28.
- Hollands, K.G.T., T.E. Unny, G.D. Raithby, and L. Konicek. 1976. Free convection heat transfer across inclined air layers. *Journal of Heat Transfer*. May:189–193.
- International Code Council. 2006. International Wildland-Urban Interface Code (Sections 504.2 and 504.3).
- Kimura, F., T. Yoshioka, K. Kitamura, M. Yamaguchi, and T. Sami. 2002. Fluid flow and heat transfer of natural convection at a slightly inclined, upward-facing, heated plate. *Heat Transfer—Asian Research*. 31(5):362–375.
- Kasuda, T. 1969. Thermal response factors for multi-layer structures of various head conduction systems. *ASHRAE Transactions* 75(1):246–271.
- Lagus, P. L., V. Kluge, P. Woods, and J. Pearson. 1988. Tracer gas testing within the Palo Verde Nuclear Generating Station Unit 3 auxiliary building. *Proceedings of the 20th NRC/DOE Air Cleaning Conference*, Boston, August.
- Miller, W.A. 2006. *The Effects of Infrared-Blocking Pigments and Deck Venting on Stone-Coated Metal Residential Roofs*. ORNL/TM-2006/9. Oak Ridge, Tennessee: Oak Ridge National Laboratory.
- Miller, W.A., J. Wilson and A. Karagiozis. 2006. The impact of above-sheathing ventilation on the thermal and moisture performance of steep-slope residential roofs and attics. Presented at the 15th Symposium on Improving Building Systems in Hot and Humid Climates, Orlando, Florida, July 24–26.
- Miller, W.A., W.M. MacDonald, A.O. Desjarlais, J.A. Atchley, M. Keyhani, R. Olson, and J. Vandewater. 2005. Experimental analysis of the natural convection effects observed within the closed cavity of tile roofs. Cool roofs: cutting through the glare. RCI Foundation Conference, May 12–13, Atlanta.
- Miller W.A., K.T. Loyle, A.O. Desjarlais, H. Akbari, R. Levinson, P. Berdahl, S. Kriner, S. Weil, and R.G. Scichili. 2004. Special IR reflective pigments make a dark roof reflect almost like a white roof. *Proceedings of ASHRAE Therm IX, the Thermal Performance of the Exterior Envelopes of Buildings IX*. December, Clearwater, Florida.
- Petrie, T.W., T.K. Stovall, and A.O. Desjarlais. 2004. Comparison of cathedralized attics to conventional attics: where and when do cathedralized attics save energy and operating costs? *Proceedings of ASHRAE Therm VIII, Thermal Performance of the Exterior Envelopes of Buildings IX*. December, Clearwater, FL.
- Quarles, S.L. and A. TenWolde. 2004. Attic and crawlspace ventilation: Implications for homes located in the Urban-Wildland Interface. *Proceedings of the Wood-*

- frame Housing Durability and Disaster Issues Conference*, Forest Products Society, October 2004. Las Vegas, Nevada.
- Rose, W.B. 1995. The history of attic ventilation regulation and research. *Proceedings of ASHRAE Therm VI, Thermal Performance of the Exterior Envelopes of Buildings VI*. Dec. 4–8. Clearwater, Florida.
- Wilkes, K.E. 1991. *Thermal Model of Attic Systems with Radiant Barriers*. ORNL/CON-262. Oak Ridge, Tennessee: Oak Ridge National Laboratory.